Graz University of Technology
Institute of Applied Mechanics

Preprint Series

Preprint No 03/2019

Generalized Convolution Quadrature based Boundary Element Method for Uncoupled Thermoelasticity

Michael Leitner, Martin Schanz
Institute of Applied Mechanics, Graz University of Technology

Published in: *Mechanical Systems and Signal Processing*
150, 107234, 2021

The final authenticated version is available online at:
https://doi.org/10.1016/j.ymssp.2020.107234

Abstract

Mechanical loads together with changing temperature conditions can be found in a wide variety of fields. Their effects on elastic media are reflected in the theory of thermoelasticity. For typical materials in engineering, very often a simplification of this coupled theory can be used, the so-called uncoupled quasistatic thermoelasticity. Therein, the effects of the deformations onto the temperature distribution is neglected and the mechanical inertia effects as well. The Boundary Element Method is used to solve numerically these equations in three dimensions. Since convolution integrals occur in this boundary element formulation, the Convolution Quadrature Method may be applied. However, very often in thermoelasticity the solution shows rapid changes and later on very small changes. Hence, a time discretisation with a variable time step size is preferable. Therefore, here, the so-called generalised Convolution Quadrature is applied, which allows for non-uniform time steps. Numerical results show that the proposed method works. The convergence behavior is, as expected, governed either by the time stepping method or the spatial discretisation, depending on which rate is smaller. Further, it is shown that for some problems the proposed use of the generalised Convolution Quadrature is the preferable.

1 Introduction

In many engineering applications not only the deformation is of interest but as well the temperature and their interaction. The presumably most prominent example are thermal stresses, i.e., the stress in an elastic body caused by a heat source or by a change in temperature. An industrial example is hot forming with all its variants. These coupled effects are described in the theory of thermoelasticity.

The theory of thermoelasticity is well known for several decades. In fact, the classical linear approach goes back to Duhamel in 1837 [14] and Neumann in 1885 [31][1]. It integrates the effects of mechanical loads together with those of a temperature field onto an elastic structure. The mathematical description is based on a system of coupled differential equations, consisting of a temperature equation and an equation for the deformations and was established by Biot [5]. The theory can be found in a variety of textbooks, see e.g., Nowacki [32]. This set of two coupled partial differential equations can be simplified by assuming that the thermoelastic dissipation can be neglected. Such an assumption results in an one-sided coupling, i.e., the temperature development is not influenced by the displacement solution but vice-versa. The other simplification is whether the inertia terms can be neglected for slow processes. Hence, four different simplifications can be found in literature. For many engineering applications, it can be assumed that the coupling of the temperature field with the displacement solution is negligible and the mechanical inertia effects can be neglected as well. This is the so called Uncoupled Quasistatic theory of Thermoelasticity (UQT), see e.g., [34], which is considered here.

For the numerical solution of this set of governing equations most numerical methods have corresponding formulations. This holds as well for the Boundary Element Method (BEM), which has gained popularity since it requires only the meshing of the body's surface. The analytical basis of a thermoelastic BEM, i.e., the respective integral representations and fundamental solutions, can be found in a series of papers by Sládek and Sládek [42, 43] and in the book of Kupradze et al. [22].

The analysis of thermoelasticity using the BEM was started by Rizzo and Shippy [35] and Cruse et al. [9]. They treated three-dimensional problems of uncoupled thermoelasticity for steady state heat conduction. BE formulations for transient thermoelasticity in 2D were presented in [45] and for 3D in [8]. First numerical results for an uncoupled formulation can be found in [41]. Further numerical results are presented for planar problems in [10] for coupled and uncoupled quasistatic thermoelasticity. Later on, the same authors showed the general three-dimensional case of UQT together with numerical results [11]. In [12], these authors show the similarities of consolidation in poroelasticity and the quasi-static thermoelasticity with numerical results. A 2D-formulation of the coupled dynamic equations has been presented in [46] using the Laplace transform and a numerical inverse transformation. By rewriting the thermal equation, a special form of the coupling term can be found which allows a formulation of the coupled quasi-static case using the elastostatic fundamental solution, i.e., partly the fundamental solutions of the uncoupled formulation [44]. An approach using particular integrals for the solution of transient

[1] This historical comment has been taken from the book [18], where further remarks and literature on the history of thermal stresses can be found.

thermoelasticity combined with the complementary solution of the steady state problem was presented by Park and Banerjee [33]. Chatterjee et al. [7] presented a simplified re-integration based fast-convolution algorithm for UQT as a memory saving alternative for large scale problems. An extension to anisotropic elastic material properties for fully coupled thermoelasticity is found in the book of Gaul [15] or in [20]. In this formulation, the dual reciprocity method is used to handle the time dependent terms.

The above discussed formulations use either a formulation in the transformed domain with an inverse transformation back to time domain, or they treat the problem in time domain directly. A methodology to compute in time domain but using Laplace domain fundamental solution is the Convolution Quadrature method (CQ), which goes back to Lubich [27, 28]. BEM formulations based on CQ can be found, e.g., for elastodynamics [19], viscoelasticity [38], and poroelasticity [39, 23]. In case of thermoelasticity, the respective formulation has been proposed in [1] with numerical results in 2D. Here, an extension is presented towards 3D, which is for the formulation of the equations straight forward. The main contribution is to allow for a variable time step size. This can be done using the so-called generalized Convolution Quadrature method (gCQ). Lopez-Fernandez and Sauter [24] published this generalisation of the CQ. The numerical realisation can be found in [25]. The extension to use a Runge-Kutta method as underlying time stepping has been presented in [26]. An application of the gCQ in acoustics with absorbing boundary conditions has been published in [36]. This extension to variable time step sizes seems to be well suited for thermoelastic problems as the solution behavior in most applications show in the beginning much larger gradients compared to later times. Hence, an adjustment of the time step size seems to be favourable.

The paper is organised as follows. First, the basic equations and relations of thermoelasticity are recapped. Next, the discretisations in space and time are introduced and the gCQ is explained. The comparison with two 1D solutions shows the performance of the method. Finally, a simplified example from hot forming shows the applicability of the proposed formulation to real world problems.

2 Uncoupled Quasistatic Thermoelasticity

The temperature field $\theta(\mathbf{x})$ and the displacement field $\mathbf{u}(\mathbf{x})$ are governed by the thermoelastic theory. This system of coupled differential equations consists of a scalar differential equation for the temperature and a vectorial differential equation for the elastic displacements. The temperature equation is similar to the heat equation but with an additional term for the influence of the mechanical heat contribution. The elastic equation is the Lamè Navier equation with a contribution accounting for the temperature influence. This fully coupled system of differential equations can be found, e.g., in [32, 22]. In many applications it is possible to neglect the influence of the displacement field on the temperature, i.e., the temperature is decoupled. Further, it is often suitable to neglect the inertia terms in the elastic equation. These simplifications result in the so called uncoupled quasistatic theory of thermoelasticity.

2.1 Differential and integral equations

Let $\Omega \subset \mathbb{R}^3$ be a bounded Lipschitz domain and $\Gamma := \partial\Omega$ its boundary with the outward normal $\mathbf{n}$. The one-sided coupled set of partial differential equations is [32]

$$\begin{aligned} \mu\nabla^2\mathbf{u}(\mathbf{x},t) + (\lambda+\mu)\nabla\nabla\cdot\mathbf{u}(\mathbf{x},t) - (3\lambda+2\mu)\ \alpha\nabla\theta(\mathbf{x},t) = 0 \\ k\nabla^2\theta(\mathbf{x},t) - \rho c_p\partial_t\theta = 0 \end{aligned} \qquad \forall(\mathbf{x},t) \in \Omega\times(0,T)\,. \tag{1}$$

The spatial derivatives are denoted with the ∇-operator with its usual meanings as grad $= \nabla$ or div $= \nabla\cdot$. The temporal derivative is denoted with ∂_t. The used material parameters are the Lamé constants λ and μ, the thermal expansion coefficient α, the thermal conductivity k, the density ρ, and the specific heat constant c_p. In (1), it is assumed that the strains are small and, consequently, a linear strain-displacement relation has been used. Further, it is assumed that the material parameters are constant. These restrictions allow to have the above set of linear partial differential equations (1), which form the basis for the following deduced boundary integral equations. The boundary Γ is split into non-overlapping sets Γ_D, Γ_N, and Γ_R such that $\Gamma = \Gamma_D \cup \Gamma_N \cup \Gamma_R$ holds. The Dirichlet, Neumann, and Robin boundary conditions are given by

$$\begin{aligned} \mathbf{u}(\mathbf{x},t) &= \mathbf{f}_D(\mathbf{x},t) && \forall\mathbf{x}\in\Gamma_D\times(0,T) \\ \theta(\mathbf{x},t) &= g_D(\mathbf{x},t) && \forall\mathbf{x}\in\Gamma_D\times(0,T) \\ \mathbf{t}(\mathbf{x},t) = \mathcal{T}^S\mathbf{u}(\mathbf{x},t) - (3\lambda+2\mu)\,\alpha\theta(\mathbf{x},t)\,\mathbf{n} &= \mathbf{f}_N(\mathbf{x},t) && \forall\mathbf{x}\in\Gamma_N\times(0,T) \\ q(\mathbf{x},t) = -k\frac{\partial}{\partial\mathbf{n}}\theta(\mathbf{x},t) &= g_N(\mathbf{x},t) && \forall\mathbf{x}\in\Gamma_N\times(0,T) \\ q(\mathbf{x},t) + \kappa(\mathbf{x})\,\theta(\mathbf{x},t) &= g_R(\mathbf{x}) && \forall\mathbf{x}\in\Gamma_R\times(0,T) \end{aligned} \tag{2}$$

where $\mathbf{t}(\mathbf{x},t)$ is the traction vector and $q(\mathbf{x},t)$ the flux. In (2), the elastic traction operator (Hooke's law) $\mathcal{T}^S\bullet = \lambda\mathbf{n}\nabla\cdot\bullet + 2\mu\frac{\partial}{\partial\mathbf{n}}\bullet + \mu\mathbf{n}\times(\nabla\times\bullet)$ has been used. Certainly, the boundary condition type, Dirichlet or Neumann, might differ in each direction of the vectorial dofs and between the elastic and thermal dofs. However, for simplifying notation this is not separately denoted. The Robin type boundary condition is mostly called convective boundary condition and in engineering usually given in the form $q(\mathbf{x},t) = -\kappa(\mathbf{x})(\theta(\mathbf{x},t) - \theta_\infty(\mathbf{x}))$ with the heat transfer coefficient κ and the ambient temperature θ_∞. In the last line of (2), a more suitable rearrangement is used with $g_R(\mathbf{x}) = \kappa(\mathbf{x})\,\theta_\infty(\mathbf{x})$. Note, the heat transfer coefficient is assumed to be independent of temperature during the calculation. This restriction allows to avoid a non-linear iterative solution.

The respective representation formula to (1) can be found in literature [22] and in a series of papers by Sládek and Sládek [42, 43]. To give a brief sketch of the derivation, the operator $\mathcal{B}$ and its adjoint $\mathcal{B}^*$ describing the governing equations (1) are introduced

$$\mathcal{B} = \begin{bmatrix} \mu\nabla^2 + (\lambda+\mu)\nabla\nabla\cdot & -(3\lambda+2\mu)\ \alpha\nabla \\ 0 & k\nabla^2 - \rho c_p\partial_t \end{bmatrix} \qquad \mathcal{B}^* = \begin{bmatrix} \mu\nabla^2 + (\lambda+\mu)\nabla\nabla\cdot & 0 \\ (3\lambda+2\mu)\ \alpha\nabla\cdot & k\nabla^2 - \rho c_p\partial_t \end{bmatrix}. \tag{3}$$

With these operators the weighted residual statement is

$$\int_0^t \int_\Omega \mathbf{G}^{\mathrm{T}}(\mathbf{x}-\mathbf{y},t-\tau)\,(\mathcal{B}\mathbf{u}^g)(\mathbf{y},\tau)\,\mathrm{d}\Omega = \int_\Omega \mathbf{G}^{\mathrm{T}}(\mathbf{x}-\mathbf{y},t) * (\mathcal{B}\mathbf{u}^g)(\mathbf{y},t)\,\mathrm{d}\Omega = 0 \tag{4}$$

where the symbol $*$ denotes the time convolution. The vector $\mathbf{u}^g = [\mathbf{u}^T\ \theta]^T$ collects the displacements and the temperature. $\mathbf{G}$ denotes the fundamental solutions defined with the adjoint operator

$$\mathcal{B}^*\mathbf{G} = \mathcal{B}^* \begin{bmatrix} \mathbf{U} & 0 \\ \mathbf{\Theta}_u^{\mathrm{T}} & \Theta \end{bmatrix} = -\begin{bmatrix} \mathbf{I} & 0 \\ 0 & \delta(t-\tau) \end{bmatrix} \delta(\mathbf{x}-\mathbf{y})\ . \tag{5}$$

The capital letters are used to mark fundamental solutions and the identity matrix is $\mathbf{I}$. In (5), $\mathbf{U}$ is the elastostatic fundamental solution, Θ the fundamental solution of the parabolic heat equation, and $\mathbf{\Theta}_u$ a coupling term, which can be found in [43] (For convenience the fundamental solutions are given in A). Performing the usual partial integrations with respect to space and time and assuming vanishing initial conditions, the representation formula ($\forall \mathbf{x} \in \Omega$)

$$\begin{bmatrix} \mathbf{u}(\mathbf{x},t) \\ \theta(\mathbf{x},t) \end{bmatrix} = -\int_0^t \int_\Omega (\mathcal{B}^*\mathbf{G})^{\mathrm{T}}(\mathbf{x}-\mathbf{y},t-\tau)\,\mathbf{u}^g(\mathbf{y},\tau)\,\mathrm{d}\Omega\,\mathrm{d}\tau = \int_\Gamma \left\{ \begin{bmatrix} \mathbf{U}(\mathbf{x}-\mathbf{y}) & -\mathbf{\Theta}_u(\mathbf{x}-\mathbf{y},t)* \\ 0 & -\Theta(\mathbf{x}-\mathbf{y},t)* \end{bmatrix} \begin{bmatrix} \mathbf{t}(\mathbf{y},t) \\ q(\mathbf{y},t) \end{bmatrix} - \begin{bmatrix} \mathbf{T}(\mathbf{x}-\mathbf{y}) & \mathbf{Q}_u(\mathbf{x}-\mathbf{y},t)* \\ 0 & Q(\mathbf{x}-\mathbf{y},t)* \end{bmatrix} \begin{bmatrix} \mathbf{u}(\mathbf{y},t) \\ \theta(\mathbf{y},t) \end{bmatrix} \right\} \mathrm{d}\Gamma \tag{6}$$

is obtained. As it is well known, the adjoint operator applied on the matrix of fundamental solutions gives the right hand side. The newly introduced fundamental solution for the tractions $\mathbf{T}(\mathbf{x}-\mathbf{y})$ is the elastostatic traction fundamental solution and $Q(\mathbf{x}-\mathbf{y},t)$ the flux fundamental solution for the heat equation (see, e.g., [6]). The fundamental solution for the coupling term $\mathbf{Q}_u(\mathbf{x}-\mathbf{y},t) = k\nabla\mathbf{\Theta}_u(\mathbf{x}-\mathbf{y},t)$ is given in [43]. The limit to the boundary with a careful consideration of the singular behavior of the fundamental solutions results in the boundary integral equation ($\forall \mathbf{x} \in \Gamma$)

$$\begin{bmatrix} \mathbf{C}(\mathbf{x}) & 0 \\ 0 & c(\mathbf{x}) \end{bmatrix} \begin{bmatrix} \mathbf{u}(\mathbf{x},t) \\ \theta(\mathbf{x},t) \end{bmatrix} = \int_\Gamma \left\{ \begin{bmatrix} \mathbf{U}(\mathbf{x}-\mathbf{y}) & -\mathbf{\Theta}_u(\mathbf{x}-\mathbf{y},t)* \\ 0 & -\Theta(\mathbf{x}-\mathbf{y},t)* \end{bmatrix} \begin{bmatrix} \mathbf{t}(\mathbf{y},t) \\ q(\mathbf{y},t) \end{bmatrix} - \begin{bmatrix} \mathbf{T}(\mathbf{x}-\mathbf{y}) & \mathbf{Q}_u(\mathbf{x}-\mathbf{y},t)* \\ 0 & Q(\mathbf{x}-\mathbf{y},t)* \end{bmatrix} \begin{bmatrix} \mathbf{u}(\mathbf{y},t) \\ \theta(\mathbf{y},t) \end{bmatrix} \right\} \mathrm{d}\Gamma\,. \tag{7}$$

Also well know, the trace operation gives an integral free term with the known expression for $\mathbf{C}$ and c from elastostatics and the heat equation, respectively. Further, the integral with $\mathbf{T}$ is only defined as Cauchy Principal Value (CPV). All other integrals are either regular or weakly singular. Note, in the second row of the matrices on the right hand side the convolution in time has to be considered opposite to the first row which is essentially the integral equation from

elastostatics. The lower line of the integral equation is the known equation for the parabolic heat equation. As seen above, the respective differential equation is decoupled and, consequently, also the integral equation. Note, the negative sign in front of the fundamental solutions $\boldsymbol{\Theta}_u$ and Θ is due to the definition of the flux as negative co-normal derivative $q = -k\partial/\partial_{\mathbf{n}}\theta$. This physically motivated definition, i.e., the negative sign, is not the mathematically suitable Neumann trace [37]. Hence, often formulations with an opposite sign and, consequently, with positive signs at the respective fundamental solutions can be found.

2.2 Spatial discretisation

Aiming at a boundary element formulation a discretisation in space and time must be introduced. First, the spatial discretisation is discussed keeping the temporal behavior continuous. The geometry description is based on a linear triangulation of the boundary, $\Gamma \approx \Gamma_h = \bigcup_e^{N_e} \tau_e$. The field variables are approximated by a linear combination of trial functions ψ_k and χ_k on these elements, which span the trial spaces

$$S_h^1(\Gamma) := \operatorname{span}\{\psi_k^1\}_{k=1}^{N_D} \quad S_h^0(\Gamma) := \operatorname{span}\{\chi_k^0\}_{k=1}^{N_N} . \tag{8}$$

The lowest order choice is applied in the following. Linear continuous trial functions $\psi_k^1 \in S_h^1(\Gamma)$ are used for the temperature and the displacements as well as piecewise constant trial functions $\chi_k^0 \in S_h^0$ for the tractions and the heat flux. Hence, the Cauchy data are approximated by

$$\mathbf{u}_h(\mathbf{x},t) = \sum_{k=1}^{N_D} \psi_k^1(\mathbf{x})\ \mathbf{u}^k(t) \quad \mathbf{t}_h(\mathbf{x},t) = \sum_{k=1}^{N_N} \chi_k^0(\mathbf{x})\ \mathbf{t}^k(t) \tag{9}$$

$$\theta_h(\mathbf{x},t) = \sum_{k=1}^{N_D} \psi_k^1(\mathbf{x})\ \theta^k(t) \quad q_h(\mathbf{x},t) = \sum_{k=1}^{N_N} \chi_k^0(\mathbf{x})\ q^k(t) . \tag{10}$$

Note, due to the different shape functions the numbers N_D and N_N differs. These shape functions are inserted together with the geometry approximation in the boundary integral equation (7). Further, a collocation approach is applied using the nodal values at the Dirichlet boundary and the element center at the Neumann boundary. The spatially discretized operators are

$$\begin{aligned}
\mathsf{V}_{[nm]} &:= \int_{\operatorname{supp}(\chi_m^0)} \mathbf{U}(\mathbf{x}_n - \mathbf{y})\ \chi_m^0(\mathbf{y})\,\mathrm{d}\Gamma_y & \mathsf{K}_{[nm]} &:= \int_{\operatorname{supp}(\psi_m^1)} \mathbf{T}(\mathbf{x}_n - \mathbf{y})\ \psi_m^1(\mathbf{y})\,\mathrm{d}\Gamma_y \\
\mathsf{V}^{\theta}_{[nm]} &:= \int_{\operatorname{supp}(\chi_m^0)} \Theta(\mathbf{x}_n - \mathbf{y},t)\ \chi_m^0(\mathbf{y})\,\mathrm{d}\Gamma_y & \mathsf{K}^{\theta}_{[nm]} &:= \int_{\operatorname{supp}(\psi_m^1)} Q(\mathbf{x}_n - \mathbf{y},t)\ \psi_m^1(\mathbf{y})\,\mathrm{d}\Gamma_y \\
\mathsf{V}^{C}_{[nm]} &:= \int_{\operatorname{supp}(\chi_m^0)} \boldsymbol{\Theta}_u(\mathbf{x}_n - \mathbf{y},t)\ \chi_m^0(\mathbf{y})\,\mathrm{d}\Gamma_y & \mathsf{K}^{C}_{[nm]} &:= \int_{\operatorname{supp}(\psi_m^1)} \mathbf{Q}_u(\mathbf{x}_n - \mathbf{y},t)\ \psi_m^1(\mathbf{y})\,\mathrm{d}\Gamma_y ,
\end{aligned} \tag{11}$$

where the square brackets $[\cdot]$ denote the discretisation indices of the matrix elements. With these operators, the two semi-discrete integral equations are

$$\mathsf{C}\,\mathsf{u}(t) = \mathsf{V}\,\mathsf{t}(t) - \mathsf{K}\,\mathsf{u}(t) + \mathsf{V}^C(t) * \mathsf{q}(t) - \mathsf{K}^C(t) * \theta(t) \tag{12a}$$

$$\mathsf{C}^{\theta}\theta(t) = \mathsf{V}^{\theta}(t) * \mathsf{q}(t) - \mathsf{K}^{\theta}(t) * \theta(t) \tag{12b}$$

The vectors $\mathsf{u},\mathsf{t},\theta$, and q hold the values of the field variables at all nodes. The jump terms are collected in the matrices C and C^θ, which depend on the boundary's geometry. The jump term for the heat equation can be found, e.g., in [2] and for elasticity in [29]. The regular integrals are computed by Gauss quadrature. Occurring weakly singular integrals are handled by a coordinate transformation, the Duffy transformation [13]. Strong singularities can be found in the elastic double layer operator K and are treated by a regularization based on partial integration [17].

To handle mixed boundary value problems, it is convenient to reorder the equation system with respect to the known and unknown data. This results in these two block equation systems

$$\begin{bmatrix} \mathsf{V}_{DD} & -\mathsf{K}_{DN}) \\ \mathsf{V}_{ND} & -(\mathsf{C}_{NN}+\mathsf{K}_{NN}) \end{bmatrix} \begin{bmatrix} \mathsf{t}_D(t) \\ \mathsf{u}_N(t) \end{bmatrix} = \begin{bmatrix} \mathsf{C}_{DD}+\mathsf{K}_{DD} & -\mathsf{V}_{DN} \\ \mathsf{K}_{ND} & -\mathsf{V}_{NN} \end{bmatrix} \begin{bmatrix} \mathsf{f}_D(t) \\ \mathsf{f}_N(t) \end{bmatrix} - \begin{bmatrix} \mathsf{f}^\theta_D(t) \\ \mathsf{f}^\theta_N(t) \end{bmatrix} \tag{13a}$$

$$\begin{bmatrix} \mathsf{V}^\theta_{DD}(t) & -\mathsf{K}^\theta_{DN})(t) \\ \mathsf{V}^\theta_{ND}(t) & -(\mathsf{C}^\theta_{NN}+\mathsf{K}^\theta_{NN})(t) \end{bmatrix} * \begin{bmatrix} \mathsf{q}_D(t) \\ \theta_N(t) \end{bmatrix} = \begin{bmatrix} \mathsf{C}^\theta_{DD}+\mathsf{K}^\theta_{DD}(t) & -\mathsf{V}^\theta_{DN}(t) \\ \mathsf{K}^\theta_{ND}(t) & -\mathsf{V}^\theta_{NN}(t) \end{bmatrix} * \begin{bmatrix} \mathsf{g}^\theta_D(t) \\ \mathsf{g}^\theta_N(t) \end{bmatrix} \tag{13b}$$

with $\mathsf{f}^\theta(t) = \mathsf{V}^C(t) * \mathsf{q}(t) - \mathsf{K}^C(t) * \theta(t)$. The indices D and N indicate that part of the boundary where the collocation point is located and where the element for the integration is.

Discrete realisation of Robin boundary conditions The Robin boundary condition in (2) is obviously a combination of Dirichlet and Neumann data. They can be handled in the BE formulation as a kind of generalised Neumann boundary condition. However, the Neumann and Dirichlet data are approximated by different discrete function spaces and must be correctly handled. Essentially, the temperature $\theta_h \in S^1_h(\Gamma_R)$ must be mapped on the function space of the flux, i.e., to a function $\bar{\theta}_h \in S^0_h(\Gamma_R)$. The discrete version of the boundary condition is

$$\mathsf{q}(\mathbf{x},t) + \kappa(\mathbf{x})\,\mathsf{R}_h\theta(\mathbf{x},t) = \mathsf{q}(\mathbf{x},t) + \kappa(\mathbf{x})\,\bar{\theta}(\mathbf{x},t) = \mathsf{g}_R \tag{14}$$

with the discretised operator matrix R_h, which maps between the different spaces. This operator matrix R_h can be found by introducing the L_2 projection (denoted by $<\cdot,\cdot>_\Gamma$)

$$\begin{aligned} \sum_k <\chi^0_\ell, \left(\psi^1_k \theta^k\right)>_{\Gamma_R} &= \sum_k <\chi^0_\ell, \left(\chi^0_k \bar{\theta}^k\right)>_{\Gamma_R} \\ \sum_k <\chi^0_\ell, \psi^1_k>_{\Gamma_R} \theta^k &= \sum_k <\chi^0_\ell, \chi^0_k>_{\Gamma_R} \bar{\theta}^k \\ \Rightarrow \mathsf{R}_h &= \sum_k <\chi^0_\ell, \chi^0_k>^{-1}_{\Gamma_R} <\chi^0_\ell, \psi^1_k>_{\Gamma_R} . \end{aligned} \tag{15}$$

For the above introduced discretisations with constant and linear approximations, the computation of (15) is cheap as the inversion of the first mass matrix $<\chi^0_\ell, \chi^0_k>_{\Gamma_R}$ can be performed locally. Further, in the above derivation a triangulation with flat elements is assumed. In this case, the Gram determinant is the same for both integrals and, hence, cancel itself.

The integral equation (13b) stays for a Robin boundary essentially the same. It results in

$$\begin{aligned} &\begin{bmatrix} \mathsf{V}^\theta_{DD}(t) & -\mathsf{K}^\theta_{DN})(t) - \mathsf{V}^\theta_{DR}(t)\,\kappa\mathsf{R}_h \\ \mathsf{V}^\theta_{ND}(t) & -(\mathsf{C}^\theta_{NN}+\mathsf{K}^\theta_{NN})(t) - \mathsf{V}^\theta_{NR}(t)\,\kappa\mathsf{R}_h \end{bmatrix} * \begin{bmatrix} \mathsf{q}_D(t) \\ \theta_N(t) \end{bmatrix} \\ &= \begin{bmatrix} \left(\mathsf{C}^\theta_{DD}+\mathsf{K}^\theta_{DD}(t)\right) * \mathsf{g}^\theta_D(t) - \mathsf{V}^\theta_{DN}(t) * \mathsf{g}^\theta_N(t) - \mathsf{V}^\theta_{DR}(t) * \mathsf{g}^\theta_R(t) \\ \mathsf{K}^\theta_{ND}(t) * \mathsf{g}^\theta_D(t) - \mathsf{V}^\theta_{NN}(t) * \mathsf{g}^\theta_N(t) - \mathsf{V}^\theta_{NR}(t) * \mathsf{g}^\theta_R(t) \end{bmatrix} . \end{aligned} \tag{16}$$

Here, the assumption of a time independent κ is used. If this assumption does not hold, a more complicated matrix structure is obtained but there is no principal problem.

Since the heat equation (13b) is independent of the elastic equation (13a), it can be solved separately, in a first step after a suitable time discretisation. Thereafter, the heat variables are known at all times and can be handled as an input quantity for the convolutions in the elastic equation, i.e., the f^{θ}-terms. This can be seen as a kind of thermal load for an elastostatic problem, which becomes time dependent due to the time dependency of the load. The time discretisation can be tackled, essentially, in three ways. Dargush and Banerjee [11] used the time domain fundamental solutions and solved the convolution integral analytically after assuming a constant time dependency within each time step. The second approach is to transform to Laplace or Fourier domain and solve the problem in the transformed domain. A very recent approach is to utilize the Convolution Quadrature Method (CQM), which has been proposed by Abreu et al. [1]. The latter will be used here as well and extended to allow for a variable time step size.

3 The Generalised Convolution Quadrature Method

The original CQM proposed by Lubich [27, 28] is restricted to a constant time step size. The generalisation to a variable step size has been developed by Lopez-Fernandez and Sauter [24], where the algorithmic realisation can be found in [25]. The extension to use a Runge-Kutta method as underlying time stepping has been presented in [26]. The following is a brief extraction from these papers.

To show the principal algorithm, a standard convolution integral is used, where the function f is replaced by its inverse Laplace transform

$$y(t) = f(t) * g(t) = \int_0^t f(t-\tau)\, g(\tau)\, \mathrm{d}\tau = \frac{1}{2\pi \mathrm{i}} \int_C \hat{f}(s) \int_0^t \mathrm{e}^{s(t-\tau)}\, g(\tau)\, \mathrm{d}\tau\ \mathrm{d}s\,, \tag{17}$$

where for the Laplace variable holds $s \in \mathbb{C}, s.t. \Re s > 0$ and C denotes the usual integration path from minus to plus infinity. The rearrangement in (17) is only valid if the Laplace transform $\hat{f}(s)$ and its inverse exist. This holds true for the kernel functions used here (see [43] for the explicit expressions). The inner time integral is the solution of the differential equation of first order

$$\frac{\partial}{\partial t} x(t,s) = s x(t,s) + g(t) \quad \text{with} \quad x(t=0,s) = 0\,. \tag{18}$$

Thus, zero initial conditions are required. This ordinary differential equation can be solved numerically by a time-stepping method. Let time steps $(t_n)_{n=0}^{N}$ be given

$$0 = t_0 < t_1 < \ldots < t_N = T \tag{19}$$

and introduce the corresponding mesh sizes $\Delta t_n = t_n - t_{n-1}$. Using the implicit Euler method for solving (18) defines the approximation

$$x_n = \frac{x_{n-1}}{1 - s\Delta t_n} + \frac{\Delta t_n}{1 - s\Delta t_n} g_n\,, \tag{20}$$

where the discrete values are the field variables at discrete times, e.g., $x_n = x(t_n)$. Inserting this approximation in (17) allows some rearrangements

$$\begin{aligned} y(t_n) &= \frac{1}{2\pi \mathrm{i}} \int_C \hat{f}(s) x_n(s) ds \\ &= \frac{1}{2\pi \mathrm{i}} \int_C \hat{f}(s) \frac{\Delta t_n}{1 - s\Delta t_n} g_n \, \mathrm{d}s + \frac{1}{2\pi \mathrm{i}} \int_C \hat{f}(s) \frac{x_{n-1}}{1 - s\Delta t_n} \mathrm{d}s \\ &= \hat{f}\left(\frac{1}{\Delta t_n}\right) g_n + \frac{1}{2\pi \mathrm{i}} \int_C \hat{f}(s) \frac{x_{n-1}}{1 - s\Delta t_n} \mathrm{d}s \, . \end{aligned} \tag{21}$$

In the last step, the condition has been used that $\hat{f}(s)$ is analytic right to the contour C. This holds for all fundamental solutions discussed in the previous section. For the remaining complex integral a quadrature formula is applied and the final quadrature formula for the convolution integral is

$$y(t_n) = \hat{f}\left(\frac{1}{\Delta t_n}\right) g_n + \sum_{\ell=1}^{N_Q} \omega_\ell \frac{\hat{f}(s_\ell)}{1 - s_\ell \Delta t_n} x_{n-1}(s_\ell) \, . \tag{22}$$

The integration points s_ℓ are distributed on a circle in the right complex half plane. These points s_ℓ and the integration weights ω_ℓ are given in C.

The above made derivation has been based on the implicit Euler method to keep the formulas simple. The extension to a Runge-Kutta method is straight forward and results, essentially, in a vector x_n of solutions at all stages of the Runge-Kutta method. Let us assume an A- and L-stable Runge-Kutta method given by its Butcher tableau $\begin{array}{c|c} \mathsf{c} & \mathsf{A} \\ \hline & \mathsf{b}^{\mathrm{T}} \end{array}$ with $\mathsf{A} \in \mathbb{R}^{m \times m}$, $\mathsf{b}, \mathsf{c} \in \mathbb{R}^m$ and m is the number of stages. The stability assumptions require that $\mathsf{b}^{\mathrm{T}} \mathsf{A}^{-1} = (0, 0, \ldots, 1)$ holds (see B for more details). With the vector $\mathbb{1} = (1, 1, \ldots, 1)^{\mathrm{T}}$ of size m and the vector g_n filled with the values of the function $g(t)$ at the stages within the time step n the algorithm is

- First step

  $$\mathsf{y}(t_1) = \hat{f}\left((\Delta t_1 \mathsf{A})^{-1}\right) \mathsf{g}_1$$

  with implicit assumption of zero initial condition.

- For all steps $n = 2, \ldots, N$ the algorithm has two steps

  1. Update the solution vector x_{n-1} at all integration points s_ℓ

     $$\mathsf{x}_{n-1}(s_\ell) = (\mathsf{I} - \Delta t_{n-1} s_\ell \mathsf{A})^{-1} \left(\left(\mathsf{b}^{\mathrm{T}} \mathsf{A}^{-1} \cdot \mathsf{x}_{n-2}(s_\ell)\right) \mathbb{1} + \Delta t_{n-1} \mathsf{A} \mathsf{g}_{n-1}\right)$$

     for $\ell = 1, \ldots, N_Q$ with the number of integration points N_Q.

  2. Compute the solution of the integral at the actual time step t_n

     $$\mathsf{y}(t_n) = \hat{f}\left((\Delta t_n \mathsf{A})^{-1}\right) \mathsf{g}_n + \sum_{\ell=1}^{N_Q} \omega_\ell \hat{f}(s_\ell) \left(\mathsf{b}^{\mathrm{T}} \mathsf{A}^{-1} \cdot \mathsf{x}_{n-1}(s_\ell)\right) (\mathsf{I} - \Delta t_n s_\ell \mathsf{A})^{-1} \mathbb{1} \tag{23}$$

As mentioned above, the parameters to be selected are given in C.

The application of formula (23) to the convolution integrals in (13) is straight forward. For the elastic equation (13a) only the contribution of the thermal load in $\mathsf{f}^{\theta}(t)$ has to be discretised, which results in

$$\begin{aligned}\mathsf{f}^{\theta}(t_n) =& \hat{\mathsf{V}}^{C}\left((\Delta t_n \mathsf{A})^{-1}\right)\mathsf{q}_n - \hat{\mathsf{K}}^{C}\left((\Delta t_n \mathsf{A})^{-1}\right)\theta_n \\ &+ \sum_{\ell=1}^{N_Q}\omega_\ell\left[\hat{\mathsf{V}}^{C}(s_\ell)\left(\mathsf{b}^{\mathsf{T}}\mathsf{A}^{-1}\cdot \mathsf{x}^{V^c}_{n-1}(s_\ell)\right) - \hat{\mathsf{K}}^{C}(s_\ell)\left(\mathsf{b}^{\mathsf{T}}\mathsf{A}^{-1}\cdot \mathsf{x}^{K^c}_{n-1}(s_\ell)\right)\right](\mathsf{I}-\Delta t_n s_\ell \mathsf{A})^{-1}\,\mathbb{1}\end{aligned} \tag{24}$$

where the upper index at $\mathsf{x}^{()}_{n-1}$ indicates that these are the results of the former step related to the operator in this upper index. Further, $\hat{()}$ at the matrices V^C and K^C denotes that in these operators the Laplace transformed fundamental solutions at the complex frequency s_ℓ are used with the exception of the actual time step where the Laplace transformed fundamental solutions at $(\Delta t_n \mathsf{A})^{-1}$ are evaluated. The application of (23) in the thermal equation (13b) gives

$$\begin{aligned}&\hat{\mathsf{M}}_1\left((\Delta t_n \mathsf{A})^{-1}\right)\begin{bmatrix}\mathsf{q}\\ \theta\end{bmatrix}_n = \hat{\mathsf{M}}_2\left((\Delta t_n \mathsf{A})^{-1}\right)\begin{bmatrix}\mathsf{g}^{\theta}_D\\ \mathsf{g}^{\theta}_N\end{bmatrix}_n \\ &+ \sum_{\ell=1}^{N_Q}\omega_\ell\left[\hat{\mathsf{M}}_2(s_\ell)\left(\mathsf{b}^{\mathsf{T}}\mathsf{A}^{-1}\cdot \mathsf{x}^{M_2}_{n-1}(s_\ell)\right) - \hat{\mathsf{M}}_1(s_\ell)\left(\mathsf{b}^{\mathsf{T}}\mathsf{A}^{-1}\cdot \mathsf{x}^{M_1}_{n-1}(s_\ell)\right)\right](\mathsf{I}-\Delta t_n s_\ell \mathsf{A})^{-1}\,\mathbb{1}\end{aligned} \tag{25}$$

with the same notation for $\mathsf{x}^{()}_{n-1}$ as above and the matrices

$$\hat{\mathsf{M}}_1 = \begin{bmatrix}\hat{\mathsf{V}}^{\theta}_{DD} & -\hat{\mathsf{K}}^{\theta}_{DN}\\ \hat{\mathsf{V}}^{\theta}_{ND} & -(\mathsf{C}^{\theta}_{NN}+\hat{\mathsf{K}}^{\theta}_{NN})\end{bmatrix} \qquad \hat{\mathsf{M}}_2 = \begin{bmatrix}\mathsf{C}^{\theta}_{DD}+\hat{\mathsf{K}}^{\theta}_{DD} & -\hat{\mathsf{V}}^{\theta}_{DN}\\ \hat{\mathsf{K}}^{\theta}_{ND} & -\hat{\mathsf{V}}^{\theta}_{NN}\end{bmatrix}.$$

To solve the thermal and the elastic system of equations, the block structure of the system matrices is used to define a Schur complement for the solution procedure. This automatically scales the different physical quantities in a mixed problem. The equation solving is performed by a direct solver, which might be replaced by a nested iterative solver for larger problems.

4 Numerical study

The above proposed thermoelastic BE formulation is applied to three examples. The first two are used for verification, whereas the third example is taken from a real world problem. The first two are by nature simple examples, essentially, a 1D solution is reproduced with the 3D BE formulation. In both cases, the load consists of a prescribed temperature and the temperature and displacement solutions are observed.

In all examples, the same material data, those of steel, are used. The specific values are given in Tab. 1. To show the effect of a variable time step size, the discretisation in time is set by

$$t_n = \left(\frac{n}{N}\right)^{\alpha} T \qquad \text{with } \alpha = 1.5 \text{ and } n = 0,\ldots,N. \tag{26}$$

λ	μ	ρ	c_p	k	α
$1.1 \cdot 10^{11}\,\mathrm{N/m^2}$	$7.3 \cdot 10^{10}\,\mathrm{N/m^2}$	$7850\,\mathrm{kg/m^3}$	$460\,\mathrm{J/K}$	$40\,\mathrm{W/mK}$	$12 \cdot 10^{-12}\,\mathrm{K^{-1}}$

Table 1: Used material data (steel S235)

This graded time mesh serves as an example and is not adjusted to the known solution behavior in the first two examples. In a real world scenario, the solution behavior can only be guessed and, hence, the time step should be adjusted adaptively. However, this is beyond the scope of this paper. The spatial discretisation is performed with linear triangles and, as mentioned above, the simplest low order shape functions, i.e., linear for the temperature and displacement and constant for traction and fluxes.

4.1 Rod under temperature load

The first example is a rod of size $3\,\mathrm{m} \times 1\,\mathrm{m} \times 1\,\mathrm{m}$ which is heated at its free side and constrained at all other sides. In Fig. 1, the geometry, boundary conditions, and one of the used meshes (the second coarsest) are displayed. The circles denote roller bearings, i.e., the normal displacements

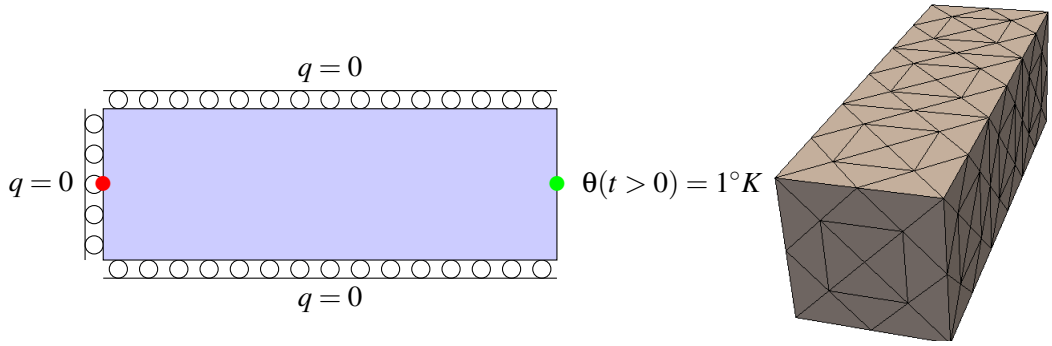

Figure 1: Geometry, boundary conditions (side view), and the mesh with $h = 0.5\,\mathrm{m}$ of the rod

are set to zero and the tangential direction is traction free. This ensures that a 1D solution is computed, i.e., 3D effects are suppressed. The analytical solutions for the temperature and displacements can be found in several papers, e.g., in [7] and are given here for convenience (L is the length of the bar)

$$\theta_{1D}(x,t) = 1 - \frac{4}{\pi}\sum_{n}^{\infty}\frac{(-1)^n}{2n+1} e^{-\frac{(2n+1)^2\pi^2 kt}{4\rho c_p L^2}} \cos\left(\frac{(2n+1)\pi x}{2L}\right) \tag{27}$$

$$u_{1D}(x,t) = \frac{3\lambda+2\mu}{\lambda+2\mu}\alpha\left(x - \frac{8L}{\pi^2}\sum_{n}^{\infty}\frac{(-1)^n}{(2n+1)^2} e^{-\frac{(2n+1)^2\pi^2 kt}{4\rho c_p L^2}} \sin\left(\frac{(2n+1)\pi x}{2L}\right)\right). \tag{28}$$

In the following, the results of the displacements at the green point (right side of the rod $x = L$) and the temperature at the red point (left side of the rod $x = 0$) are computed and compared to the analytical solution. In Fig. 2, the computed temperature is plotted versus time, where

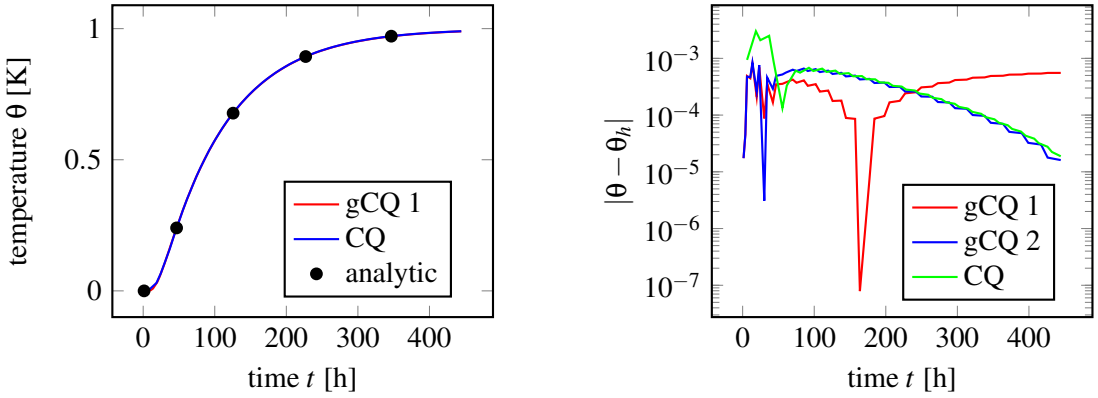

(a) Temperature

(b) Pointwise error

Figure 2: Temperature at the fixed end versus time. gCQ 1 is computed with $N_Q = N\log^2(N)$ and gCQ 2 with $N_Q = N\log^3(N)$

CQ denotes results using a constant time step size. The results marked gCQ 1 are computed with a variable time step size following (26) and $N_Q = N\log^2(N)$, whereas gCQ 2 means the same variable time step size but $N_Q = N\log^3(N)$. In all computations shown in Fig. 2 a 2-stage Radau IIA method (see B) is used and a mesh with 3548 elements. All other parameters of the computations can be found in Tab. 2. Figure 2a shows the comparison of the CQ and gCQ results with the analytical solution. The agreement is very good. The error plot presented in Fig. 2b shows that for earlier times the variable time step size is superior. The large time behavior is the same for the CQ and the gCQ as long as a sufficient amount of frequencies N_Q are used, i.e., the solution gCQ 2. Nevertheless, also the solution gCQ 1 has an acceptable error for larger times. In this solution less frequencies are used which makes it computational advantageous. For the displacement solution, very similar plots could be made, where exactly the same tendency is found. Hence, these plots are skipped.

To see the behavior of the numerical method, the error measured with

$$\text{error}_2 = \frac{1}{N}\sqrt{\sum_{n=0}^{N} \Delta t_n \left|\mathbf{u}(\mathbf{x},t_n) - \mathbf{u}_h(\mathbf{x},t_n)\right|^2} \tag{29}$$

$$\text{error}_{max} = \max_{1\le n\le N} \left|\mathbf{u}\left(\mathbf{x}, \frac{t_n + t_{n-1}}{2}\right) - \mathbf{u}_h\left(\mathbf{x}, \frac{t_n + t_{n-1}}{2}\right)\right| \tag{30}$$

is studied. It must be remarked that due the pointwise nature of the 1D solution also the error measure can only be pointwise, i.e., at only one single point. The error (29) is an approximation of the L_2-error in time and (30) is the maximum error in time. The approximated BE solution is denoted with $\mathbf{u}_h$, whereas $\mathbf{u}$ means the exact solution. For the temperature, the analogous error definition is used. To see the convergence behavior, the spatial and temporal discretisation has been refined by an uniform refinement. The respective values of the numbers of elements, time steps and their sizes can be found in Tab. 2. As underlying time stepping method, the backward differential formula of order 1 (BDF 1) and a 2-stage Radau IIA method with $N_Q = N\log^2(N)$

Elements	h	N (BDF 1)	N (Radau IIA2)	Δt_{const} (BDF 1)	Δt_{const} (Radau IIA2)
56	1	6	3	266666	533333
224	0.5	12	6	133333	266666
896	0.25	24	12	66666	133333
3584	0.125	48	24	33333	66666
14336	0.0625	96	48	16666.7	33333.3

Table 2: Data for the refined meshes of the rod (Δt in seconds)

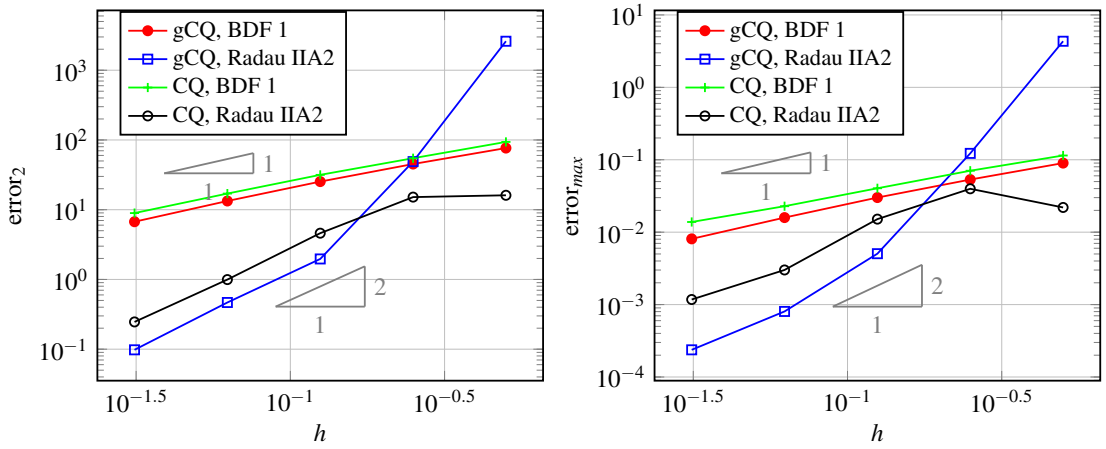

(a) L_2-error in time

(b) Maximum error in time

Figure 3: Pointwise error for the temperature solution at the fixed end

is used. A higher value of N_Q does not change the following results significantly. To have a fair comparison, the step size in the BDF 1 is chosen half of the 2-stage method. Hence, the numerical effort for both methods are comparable. However, it is expected that the 2-stage method shows a higher convergence order. It must be mentioned that the comparison is not a strict convergence study as it is observed only at one point (see the comment on the piecewise error above) and the analytical solution is only 1D and not a solution of the 3D problem. Nevertheless, the results show how the proposed method behaves and the difference of the CQ to the gCQ. In Fig. 3, the rates for the temperature solution are presented and the respective results for the displacements can be found in Fig. 4.

It must be remarked that the x-labels in the plots in Fig. 3 and Fig. 4 are somehow misleading as not only the spatial mesh is refined but as well the temporal. Hence, the ratio spatial mesh size to the time step size is kept constant. The essential conclusion of these results is that the expected convergence rate can be achieved. It can be observed that the convergence rates are determined either by the spatial discretisation or by the underlying time stepping method. The BDF 1 allows in maximum order one and the 2-stage Radau IIA could achieve order three. But, the linear spatial discretisation of the Dirichlet data restrict the convergence rate to two. Based on these considerations, it can be concluded that the expected convergence rates are obtained.

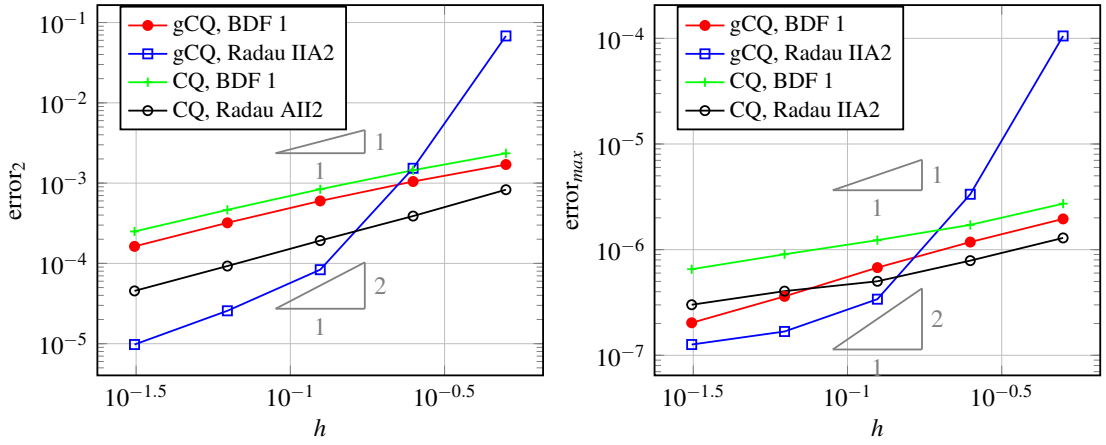

(a) L_2-error in time

(b) Maximum error in time

Figure 4: Pointwise error for the displacement solution at the free end

Further, it is observed that the error level of the gCQ is smaller if a sufficient small h is used, i.e. the gCQ has a smaller constant in the error compared to the CQ solution. This was already expected from the error plot in Fig. 2b.

These observations can be clearly identified for the L_2 error in time (29) but are not that obvious for the maximum error (30). In Fig. 4b, the rates for the displacement solutions are not as close to order two as for the temperature. This might have several reasons as, e.g., an 1D solution is compared to a 3D solution. This is more critical for the displacements as the lateral displacements have some values not equal to zero, which are small compared to the longitudinal values, but still spoil the results.

4.2 Solid sphere

The second example can as well be found in other publications as a kind of benchmark. It is a sphere with radius 1 m loaded by a temperature jump. The surface is traction free. An analytical solution can be found, e.g., in [33] and [32]. It is essentially a radial symmetric solution, which is modelled here with the 3D BE formulation. The problem setting is in principle a pure Neumann problem for the elastostatic part of the governing equations, which causes trouble. However, in the numerical model only one eighth of the sphere is discretised with symmetry boundary conditions. These boundary conditions fix the center of the sphere and, hence, the problem is no longer a pure Neumann problem. This ensures the solvability of the problem and reduces the problem size. In Fig. 5, the geometry, boundary conditions, and the second coarsest mesh with 64 elements are presented. As before, first the solution and the error over time are discussed. In Fig. 6, the displacement solution in radial direction is plotted versus time. The green point in figure 5 marks the evaluation point on the surface of the sphere. Also for this problem, the displacement and temperature BE solutions show the same behavior. Hence, only the displacement solutions are presented. The results in Fig. 6 indicate that the error of the gCQ solution is mostly smaller than that of the CQ solution. These results are obtained with

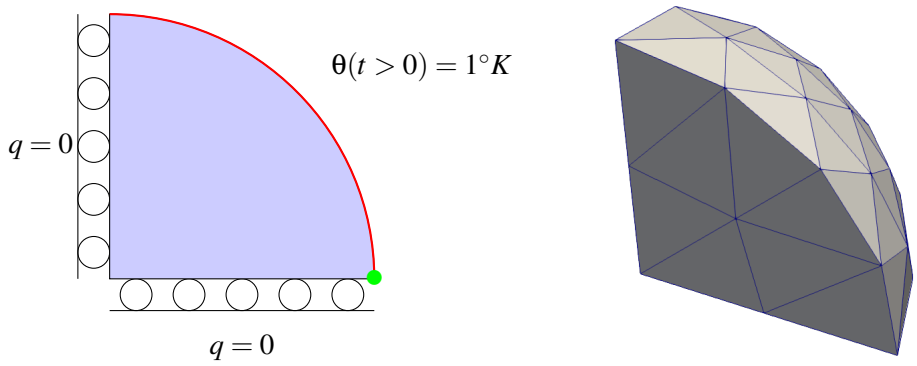

Figure 5: Geometry, boundary conditions (side view), and the mesh with $h = 0.5\,\mathrm{m}$ for the sphere

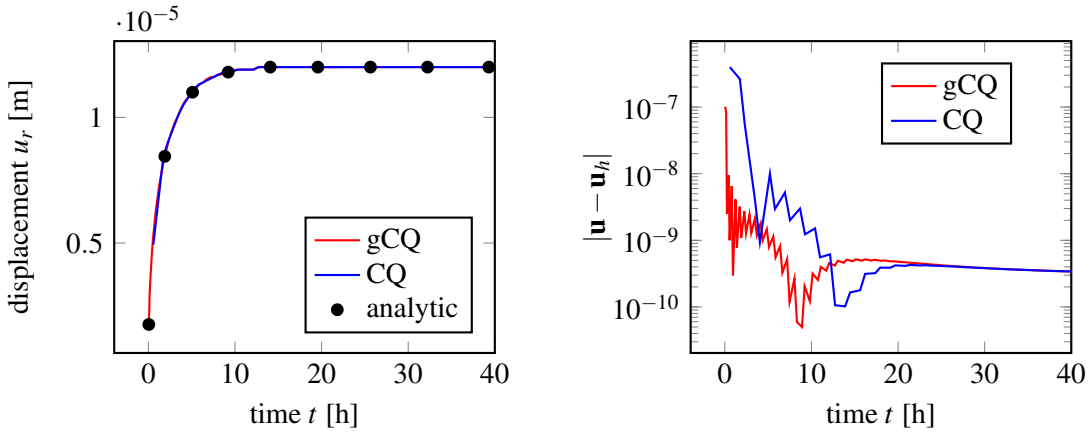

(a) Displacement

(b) Spatial L_2-error

Figure 6: Displacement at the surface of the sphere versus time

$N_Q = N \log^2(N)$.

For the convergence study, an initial very coarse mesh is uniformly refined by bisection of the hypothenuse of the triangles. The displayed mesh in Fig. 5 is obtained after the first refinement step. The respective time step size is as well refined with the spatial mesh, i.e., the ratio of time step size to mesh size is kept constant. The respective data can be found in Tab. 3.

The errors are studied for the temperature and the displacement solution. The same notation and time stepping methods as in section 4.1 are used and it is expected to get similar results. But, it must be remarked that different to the rod, here, an additional error appears, the discretisation error of the geometry. Flat linear triangles are used to approximate the sphere, which is for the coarse meshes a crude approximation. Nevertheless, the error level is comparable to the rod example. Different to the rod problem above, here, a true L_2-error in the spatial variable can be

N	h	N (BDF 1)	N (Radau IIA2)	Δt_{const} (BDF 1)	Δt_{const} (Radau IIA2)
16	1	16	50000	8	100000
64	0.5	32	25000	16	50000
256	0.25	64	12500	32	25000
1024	0.125	128	6250	64	12500
4096	0.0625	256	3125	128	6250

Table 3: Data for the refined meshes of the sphere (Δt in seconds)

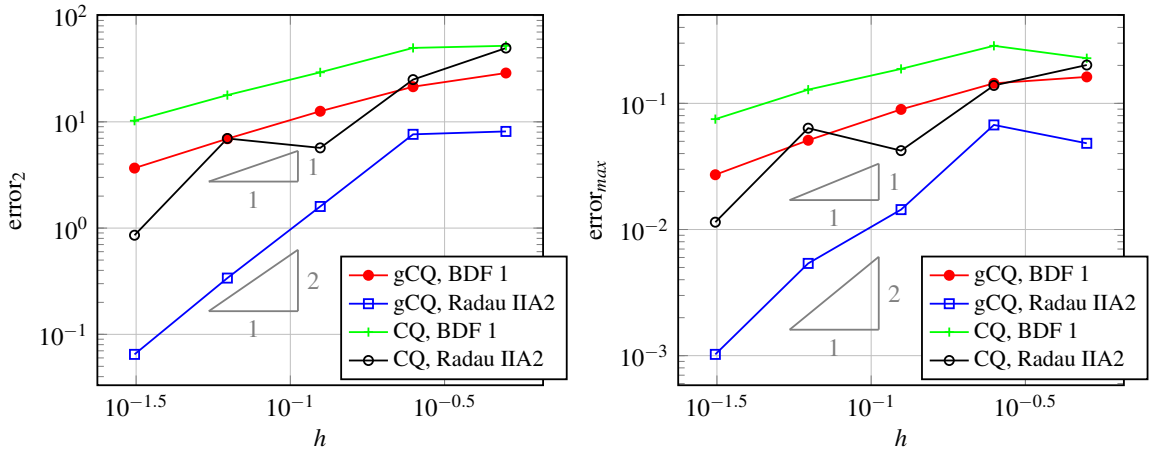

(a) L_2-error in time (b) Maximum error in time

Figure 7: Error for the temperature solution of the sphere

studied. The used error measures are

$$\text{error}_2 = \frac{1}{N}\sqrt{\sum_{n=0}^{N} \Delta t_n \|\mathbf{u}(\mathbf{x},t_n) - \mathbf{u}_h(\mathbf{x},t_n)\|^2_{L_2(\Gamma)}} \tag{31}$$

$$\text{error}_{max} = \max_{1\le n\le N} \|\mathbf{u}\left(\mathbf{x}, \frac{t_n + t_{n-1}}{2}\right) - \mathbf{u}_h\left(\mathbf{x}, \frac{t_n + t_{n-1}}{2}\right)\|_{L_2(\Gamma)}\,. \tag{32}$$

In Fig. 7 and Fig. 8, these two errors are plotted for the temperature and displacement solution, respectively. As anticipated, the overall behavior is the same. However, the maximum error in time shows for the displacement solution only a linear behavior. The temperature solution and the L_2 errors in time show, as expected, a linear order for BDF 1 and a quadratic order for the 2-stage Radau IIA method. One reason for the breakdown in Fig. 8b might be that the error introduced by the geometry approximation is dominating. Nevertheless, without a mathematical analysis this effect cannot be clarified. From an engineering point of view, the method seems to be suitable to be used with an acceptable error behavior.

Remark 1. The presented results show some advantages of the gCQ compared to the CQ. However, as usual in numerics this flexibility to adapt the time step size is not for free. From the determination of N_Q (see C) it is clear that more BE calculations have to be performed for the

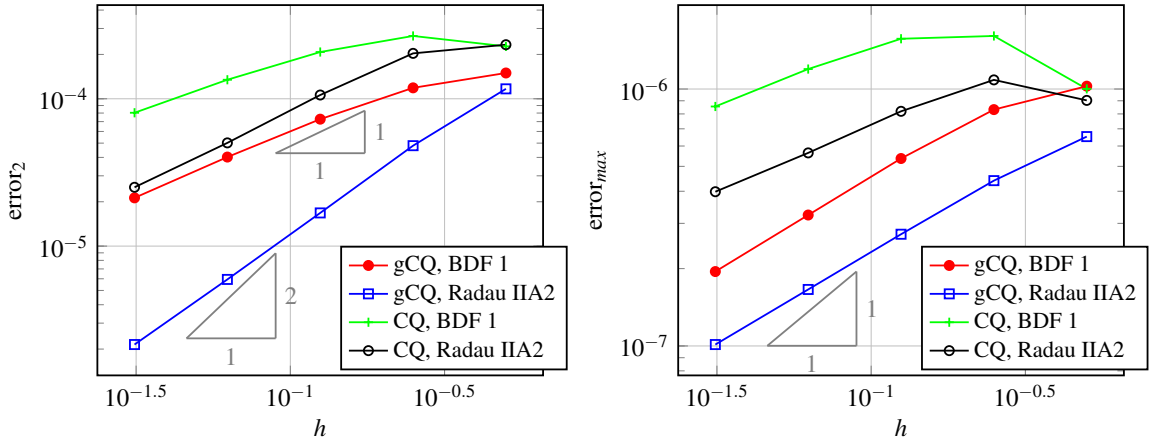

(a) L_2-error in time

(b) Maximum error in time

Figure 8: Error for the displacement solution of the sphere

gCQ compared to the CQ if the same N is assumed. But, if much less time steps are necessary due to a coarsening of the step size, there may exist a situation where the gCQ is computational advantageous. A more severe drawback of gCQ is that the algorithm is inherently sequential with the exception of the computation of the system matrices. The CQ can be performed easily in parallel as long as it is set up as proposed in [3]. But for large systems this realisation with one equation solve per complex frequency may become slow without an efficient preconditioner. This is different for the gCQ, where the equation solve is done in time domain with a nearly sparse matrix. Nevertheless, both methods need fast BE methods to work for large real world problems.

4.3 Hot forming tool

The last example is to demonstrate that also realistic modells can be computed with the proposed method. The example is taken from hot forming processes as they occur, e.g., in car production. The main interest in such a simulation is the form of the deformed metal sheet and its material properties. Both points are not considered here, but the tool itself is simulated. Those tools should not deform and steer the cooling process within the sheet. Hence, the challenging task is to locate the cooling channels such that the required material properties in the sheet can be obtained. This results in an highly complicated geometry of the tool. The temperature and the deformation of the tool can be approximated by a linear theory, hence, the proposed method is applicable.

In the following, the tool displayed in Fig. 9 is considered. The influence of the sheet on the tool is modelled with a Robin boundary condition, where the heat transfer coefficient $\kappa(\mathbf{x})$ is determined by an energy estimate as proposed in [21, 47]. This approached has been verified experimentally in these papers. As well, the temperature solution of a purely thermal calculation has been checked against the measured data with a reasonable agreement [30]. The new part here is the deformation in the coupled computation. The sheet has a temperature of $750\,^oC$ at the time

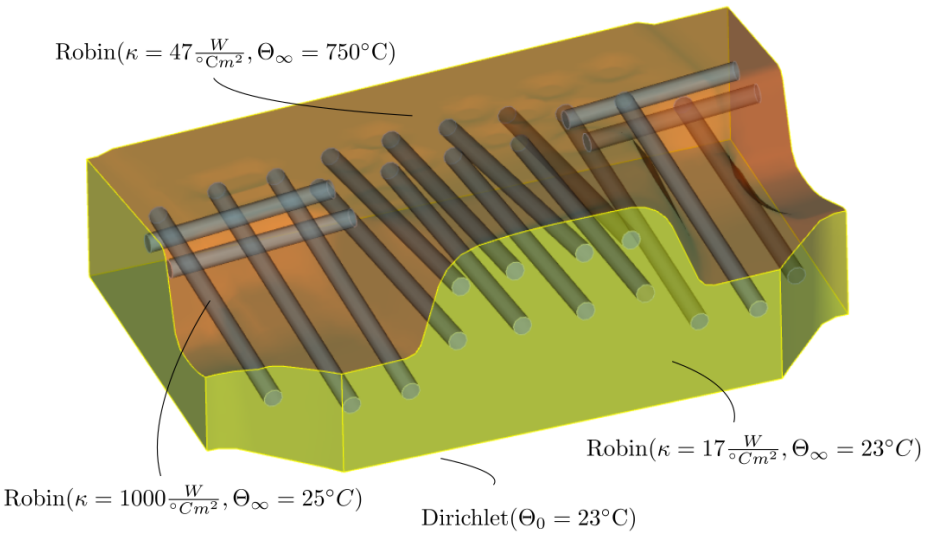

Figure 9: Forming tool with the prescribed boundary conditions

of contact with the tool. At the bottom, room temperature is assumed. In the channels and on the front side, as well convective boundary conditions are set. The material data of the tool are listed in Tab. 1. The time is discretised with a variable time step size following (26) using $\alpha = 1.5, T = 120\,\mathrm{s}$, and $N = 30$. Again, a 2-stage Radau IIA method is used within the gCQ and the spatial discretisation is performed with linear triangles. The shape functions are chosen as before, linear for the Dirichlet data and constant for the Neumann data.

The screenshots in Fig. 10 show the temperature distribution and the norm of the displacements on the tool at the end time ($T = 120\,\mathrm{s}$) of the simulation. Aside, the temperature and displacement behavior with respect to time is shown. Certainly, the results can only be ranked as reasonable without a reference solution. The displacements are well below the millimetre range and the temperature is up to $72\,^oC$. The graphs of the variation in time for the temperature and displacements at a point on the surface are as well reasonable. The large displacements around one millimetre showing up at some points are presumably numerical artifacts as they appear on the cooling channels. These circular channels are approximated by a minimum of flat triangles. A better mesh resolution would most probably eliminate these peaks in the displacement distribution. Unfortunately, without compression techniques the used spatial mesh is the largest for the available computing facilities.

5 Conclusions

A boundary element formulation for uncoupled themoelasticity has been proposed. Different to existing formulations, here, the generalised Convolution Quadrature method (gCQ) is used for time discretisation and, therefore, a variable time step size is possible. Also, Robin type boundary conditions, i.e., convective boundary conditions, have been realised via a modified

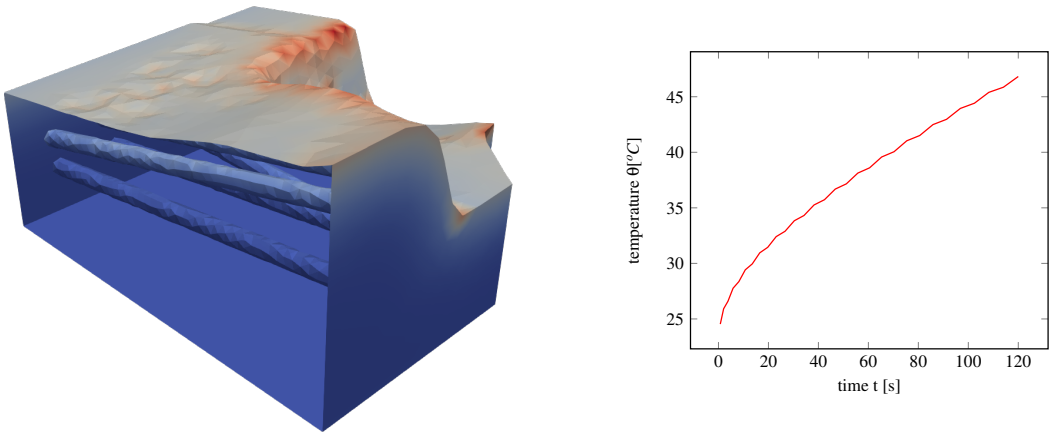

(a) Temperature: blue 20 ^oC, red 72 ^oC

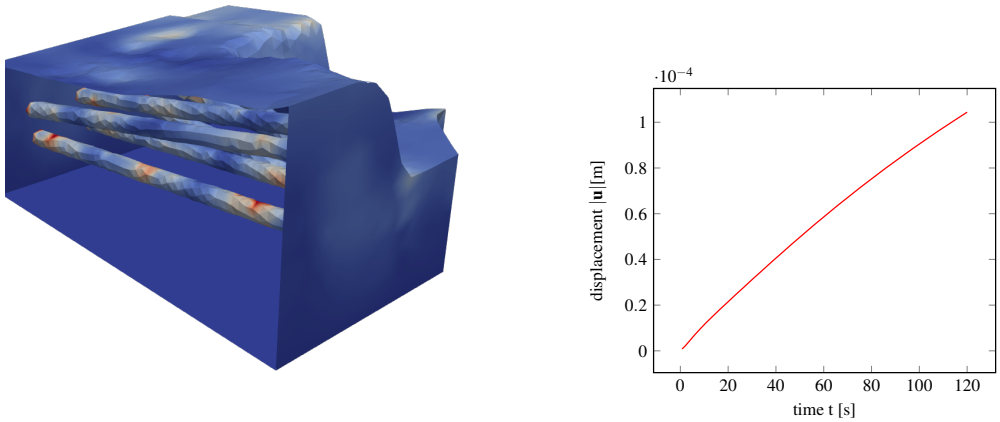

(b) Displacement: blue 0 mm, red 1 mm

Figure 10: Temperature and displacement distribution in the hot forming tool

Neumann boundary condition. The results show, first, the proposed method works. Second, the convergence behavior is as expected governed either by the spatial discretisation or by the temporal discretisation. The rates are the same as in the corresponding elliptic problem if the temporal discretisation is sufficiently good. Essentially, a higher order Runge-Kutta method should be used within the gCQ. Further, if the problem has strong gradients in the temporal solution a variable time step size pays off. Last, it is shown that also real world problems can be handled with the proposed method. Certainly, without using fast methods the applicability is restricted as in all 3D BE formulations. But the structure of the gCQ allows for an application of either $\mathcal{H}$-matrices with adaptive cross approximation or the fast multipole method based on a Chebyshev expansion.

Acknowledgement The authors gratefully acknowledge the financial support by the Austrian Science Fund (FWF) under Grant P 25557-N30.

A Fundamental solutions

The fundamental solution tensors corresponding to the adjoint operator in (5) can be found in literature, e.g., [43]. One part is the elastostatic fundamental solution, i.e., the displacement solution due to a mechanical load (an impulse)

$$U_{ij} = \frac{1}{8\pi r}\frac{1}{\mu(\lambda+2\mu)}\left[\delta_{ij}(\lambda+3\mu)+(\lambda+\mu)r_{,i}r_{,j}\right] . \tag{33}$$

The temperature caused by a mechanical load is

$$(\Theta_u)_i = \frac{(3\lambda+2\mu)\alpha}{(\lambda+2\mu)}\frac{r_{,i}}{4\pi s\rho c_p r}\left[\left(\sqrt{s\frac{\rho c_p}{k}}+\frac{1}{r}\right)\mathrm{e}^{-\sqrt{s\frac{\rho c_p}{k}}r}-\frac{1}{r}\right] \tag{34}$$

the temperature caused by a heat source

$$\Theta = \frac{1}{4\pi r k}\mathrm{e}^{-\sqrt{s\frac{\rho c_p}{k}}r} . \tag{35}$$

The solution for the tractions is as well that of elastostatics

$$\begin{aligned} T_{ij} &= \mu\left(U_{ij,k}+U_{kj,i}\right)n_k+\lambda U_{kj,k}n_i \\ &= \frac{-1}{4\pi(\lambda+2\mu)r^2}\left\{\left[\mu\delta_{ij}+(\lambda+\mu)3r_{,i}r_{,j}\right]r_{,n}-\mu\left(r_{,i}n_j-r_{,j}n_i\right)\right\} \end{aligned} \tag{36}$$

and the (adjoint) fluxes are

$$Q = \frac{-r_{,n}}{4\pi r}\left(\sqrt{s\frac{\rho c_p}{k}}+\frac{1}{r}\right)\mathrm{e}^{-\sqrt{s\frac{\rho c_p}{k}}r} \tag{37}$$

$$\begin{aligned} (Q_u)_i = \frac{(3\lambda+2\mu)\alpha}{(\lambda+2\mu)}\frac{k}{4\pi s\rho c_p r}\Bigg[&\left(\frac{\mathrm{e}^{-\sqrt{s\frac{\rho c_p}{k}}r}}{r}\left(\sqrt{s\frac{\rho c_p}{k}}+\frac{1}{r}\right)-\frac{1}{r^2}\right)(n_i-3r_{,i}r_{,n}) \\ &-s\frac{\rho c_p}{k}\mathrm{e}^{-\sqrt{s\frac{\rho c_p}{k}}r}r_{,i}r_{,n}\Bigg] . \end{aligned} \tag{38}$$

B Runge-Kutta methods in gCQ

A comprehensive presentation of Runge-Kutta methods may be found in the book by Hairer and Wanner [16].

Let a Runge-Kutta method of (classical) order p and stage order q be given by its Butcher tableau $\begin{array}{c|c} \mathsf{c} & \mathsf{A} \\ \hline & \mathsf{b}^{\mathsf{T}} \end{array}$ with $\mathsf{A} \in \mathbb{R}^{m\times m}$, $\mathsf{b},\mathsf{c} \in \mathbb{R}^m$ and m is the number of stages. A Runge-Kutta method is said to be A-stable if the stability function

$$R(z) = 1 + z\mathbf{t}\,(\mathsf{I} - z\mathsf{A})^{-1}\,\mathbb{1}, \qquad \mathbb{1} := (1,1,\ldots,1)^T, \tag{39}$$

is bounded as

$$|R(z)| \le 1, \quad \text{for } \Re z \le 0 \text{ and } \mathsf{I} - z\mathsf{A} \text{ is non-singular for all } \Re z \le 0. \tag{40}$$

The experience with the multistep based CQ in the application on BEM shows that the assumption of A-stability is necessary (see, e.g., [40]). In order to be able to make use of the convergence results proved in [4], the following assumptions will be made on the Runge-Kutta method:

1. The Runge-Kutta method is A-stable with (classical) order $p \ge 1$ and stage order $q \le p$.
2. The stability function satisfies $|R(\mathrm{i}y)| < 1$ for all real $y \ne 0$.
3. $R(\infty) = 0$.
4. The Runge-Kutta coefficient matrix A is invertible.

To simplify expressions assume further that $\mathsf{b}^{\mathsf{T}}\mathsf{A}^{-1} = (0,0,\ldots,1)$ holds, i.e., that the method is stiffly accurate [16] or also called L-stable. This in turn implies that $c_m = 1$. Radau IIA and Lobatto IIIC are examples of Runge-Kutta methods satisfying all of the above conditions (see Tab. 4 for their Butcher tableaus). In a Runge-Kutta method computations are done not only at the equally spaced points $t_n = n\Delta t$ but also at the stages $t_n + c_\ell \Delta t$, $\ell = 1,2,\ldots,m$. Note that $c_m = 1$ implies $t_n + c_m\Delta t = t_{n+1}$.

C Parameter for the gCQM

The derivation and reasoning how the integration weights and points are determined can be found in [25, 26]. The result of these papers are recalled here. The integration points in the complex plane are

$$s_\ell = \gamma(\sigma_\ell)\,, \qquad \omega_\ell = \frac{4K(k^2)}{1\pi i}\gamma'(\sigma_\ell)\,, \qquad N_Q = N\log(N)\,,$$

where for Runge-Kutta methods with stages $m > 1$ it should be $N_Q = N\log^2(N)$ or sometimes $N_Q = N\log^3(N)$. $K(k)$ is the complete elliptic integral of first kind

$$K(k) = \int_0^1 \frac{dx}{\sqrt{(1-x^2)(1-k^2x^2)}}\,, \qquad K'(k) = K(1-k)$$

$$\begin{array}{c|cc} \frac{1}{3} & \frac{5}{12} & -\frac{1}{12} \\ 1 & \frac{3}{4} & \frac{1}{4} \\ \hline & \frac{3}{4} & \frac{1}{4} \end{array}$$

(a) 2-stage Radau IIA

$$\begin{array}{c|cc} 0 & \frac{1}{2} & -\frac{1}{2} \\ 1 & \frac{1}{2} & \frac{1}{2} \\ \hline & \frac{1}{2} & \frac{1}{2} \end{array}$$

(b) 2-stage Lobatto IIIC

$$\begin{array}{c|ccc} \frac{4-\sqrt{6}}{10} & \frac{88-7\sqrt{6}}{360} & \frac{296-169\sqrt{6}}{1800} & \frac{-2+3\sqrt{6}}{225} \\ \frac{4+\sqrt{6}}{10} & \frac{296+169\sqrt{6}}{1800} & \frac{88+7\sqrt{6}}{360} & \frac{-2-3\sqrt{6}}{225} \\ 1 & \frac{16-\sqrt{6}}{36} & \frac{16+\sqrt{6}}{36} & \frac{1}{9} \\ \hline & \frac{16-\sqrt{6}}{36} & \frac{16+\sqrt{6}}{36} & \frac{1}{9} \end{array}$$

(c) 3-stage Radau IIA

$$\begin{array}{c|ccc} 0 & \frac{1}{6} & -\frac{1}{3} & \frac{1}{6} \\ \frac{1}{2} & \frac{1}{6} & \frac{5}{12} & -\frac{1}{12} \\ 1 & \frac{1}{6} & \frac{2}{3} & \frac{1}{6} \\ \hline & \frac{1}{6} & \frac{2}{3} & \frac{1}{6} \end{array}$$

(d) 3-stage Lobatto IIIC

Table 4: Butcher tableaus of *A*- and *L*-stable Runge-Kutta methods

and K' is its derivative, which equals the integral of the complementary modulus. The argument k depends on the relation q of the maximum and minimum step sizes in the following way

$$k = \frac{q - \sqrt{2q-1}}{q + \sqrt{2q-1}} \qquad q = \frac{\Delta t_{\max} 5 \max_i |\lambda_i(\mathsf{A})|}{\Delta t_{\min} \min_i |\lambda_i(\mathsf{A})|} ,$$

with the eigenvalues $\lambda_i(\mathsf{A})$. For the implicit Euler, i.e., a one stage Runge-Kutta method, the eigenvalues are 1 and the factor 5 in q can be skipped. The functions $\gamma(\sigma_\ell)$ and $\gamma'(\sigma_\ell)$ are

$$\begin{aligned} \gamma(\sigma_\ell) &= \frac{1}{\Delta t_{\min}(q-1)} \left(\sqrt{2q-1} \frac{k^{-1} + \mathrm{sn}(\sigma_\ell)}{k^{-1} - \mathrm{sn}(\sigma_\ell)} - 1 \right) , \\ \gamma'(\sigma_\ell) &= \frac{\sqrt{2q-1}}{\Delta t_{\min}(q-1)} \frac{2\,\mathrm{cn}(\sigma_\ell)\,\mathrm{dn}(\sigma_\ell)}{k(k^{-1} - \mathrm{sn}(\sigma_\ell))^2} , \\ \sigma_\ell &= -K(k^2) + \left(\ell - \frac{1}{2} \right) \frac{4K(k^2)}{N_Q} + \frac{i}{2} K'(k^2) , \end{aligned}$$

where $\mathrm{sn}(\sigma_\ell)$, $\mathrm{cn}(\sigma_\ell)$ and $\mathrm{dn}(\sigma_\ell)$ are the Jacobi elliptic functions. As seen from above, the integration contour is only determined by the largest and the smallest time steps chosen but not dependent on any intermediate step sizes. Due to the symmetric distribution of the integration points with respect to the real axis, only half of the frequencies s_ℓ need to be calculated.

References

[1] A. I. Abreu, A. Canelas, B. Sensale, and W. J. Mansur. Cqm-based BEM formulation for uncoupled transient quasistatic thermoelasticity analysis. *Eng. Anal. Bound. Elem.*, 36 (4):568–578, 2012. ISSN 0955-7997. doi: 10.1016/j.enganabound.2011.10.003. URL `http://www.sciencedirect.com/science/article/pii/S0955799711002311`.

[2] M. H. Aliabadi. *The Boundary Element Method: Applications in Solids and Structures*, volume 2. J. Wiley & Sons, 2002.

[3] L. Banjai and S. Sauter. Rapid solution of the wave equation in unbounded domains. *SIAM J. Numer. Anal.*, 47(1):227–249, 2008.

[4] L. Banjai, C. Lubich, and J. M. Melenk. Runge-Kutta convolution quadrature for non-sectorial operators arising in wave propagation. *Numer. Math.*, 119(1):1–20, 2011. doi: 10.1007/s00211-011-0378-z.

[5] M. A. Biot. Thermoelasticty and irreversible thermodynamics. *J. Appl. Phys.*, 27(3):240–253, 1956.

[6] C. A. Brebbia, J. C. F. Telles, and L. C. Wrobel. *Boundary Element Techniques*. Springer-Verlag, Berlin, New York, 1984.

[7] J. Chatterjee, F. Ma, D. P. Henry, and P. K. Banerjee. Two- and three-dimensional transient heat conduction and thermoelastic analyses by BEM via efficient time convolution. *Comput. Methods Appl. Mech. Engrg.*, 196(29–30):2828–2838, 2007.

[8] A. Chaudouet. Three-dimensional transient thermo-elastic analyses by the BIE method. *Int. J. Numer. Methods. Engrg.*, 24(1):25–45, 1987. doi: 10.1002/nme.1620240103. URL https://onlinelibrary.wiley.com/doi/abs/10.1002/nme.1620240103.

[9] T. A. Cruse, D. W. Snow, and R. B. Wilson. Numerical solutions in axisymmetric elasticity. *Comput. & Structures*, 7(3):445–451, 1977. ISSN 0045-7949. doi: https://doi.org/10.1016/0045-7949(77)90081-5. URL http://www.sciencedirect.com/science/article/pii/0045794977900815.

[10] G. F. Dargush and P. K. Banerjee. Development of a boundary element method for time-dependent planar thermoelasticity. *Internat. J. Solids Structures*, 25(9):999–1021, 1989. ISSN 0020-7683. doi: https://doi.org/10.1016/0020-7683(89)90018-8. URL http://www.sciencedirect.com/science/article/pii/0020768389900188.

[11] G. F. Dargush and P. K. Banerjee. Boundary element methods in three-dimensional thermoelasticity. *Internat. J. Solids Structures*, 26(2):199–216, 1990. ISSN 0020-7683. doi: 10.1016/0020-7683(90)90052-W. URL http://www.sciencedirect.com/science/article/pii/002076839090052W.

[12] G. F. Dargush and P. K. Banerjee. A new boundary element method for three-dimensional coupled problems of consolidation and thermoelasticity. *J. of Appl. Mech.*, 58(1):28–36, 03 1991. ISSN 0021-8936. doi: 10.1115/1.2897169. URL https://doi.org/10.1115/1.2897169.

[13] M. G. Duffy. Quadrature over a pyramid or cube of integrands with a singularity at a vertex. *SIAM J. Numer. Anal.*, 19(6):1260–1262, 1982.

[14] J.-M.-C. Duhamel. Second mémoire sur les phénomènes thermo-mécaniques. *J. de l'Ecole Polytechnique*, 15(25):1–57, 1837.

[15] L. Gaul, M. Kögl, and M. Wagner. *Boundary Element Methods for Engineers and Scientists*. Springer, 2003.

[16] E. Hairer and G. Wanner. *Solving Ordinary Differential Equations II: Stiff and Differential-Algebraic Problems*. Springer Series in Computational Mathematics. Springer-Verlag, Berlin Heidelberg, 1991.

[17] H. Han. The boundary integro-differential equations of three-dimensional Neumann problem in linear elasticity. *Numer. Math.*, 68(2):269–281, 1994.

[18] Richard B. Hetnarski and M. Reza Eslam. *Thermal Stresses – Advanced Theory and Applications*, volume 158 of *Solid mechanics and its applications*. Springer, 2009.

[19] L. Kielhorn and M. Schanz. Convolution quadrature method based symmetric Galerkin boundary element method for 3-d elastodynamics. *Int. J. Numer. Methods. Engrg.*, 76(11): 1724–1746, 2008.

[20] M. Kögl and L. Gaul. A boundary element method for anisotropic coupled thermoelasticity. *Arch. Appl. Mech.*, 73:377–398, 2003.

[21] R. Kolleck, H. Löscher, W. Weiß, and R. Veit. Alternative approaches for the simulation of the hot forming process. In P. Hora, editor, *7th International Conference and Workshop on Numerical Simulation of 3D Sheet Metal Forming Processes (Numisheet)*, pages 621–626, 2008.

[22] V. D. Kupradze, T. G. Gegelia, M. O. Basheleishvili, and T. V. Burchuladze. *Three-Dimensional Problems of the Mathematical Theory of Elasticity and Thermoelasticity*, volume 25 of *Applied Mathematics and Mechanics*. North-Holland, Amsterdam New York Oxford, 1979.

[23] P. Li and M. Schanz. Time domain boundary element formulation for partially saturated poroelasticity. *Eng. Anal. Bound. Elem.*, 37(11):1483–1498, 2013. doi: 10.1016/j.enganabound.2013.08.002.

[24] M. Lopez-Fernandez and S. Sauter. Generalized convolution quadrature with variable time stepping. *IMA J. of Numer. Anal.*, 33(4):1156–1175, 2013. doi: 10.1093/imanum/drs034.

[25] M. Lopez-Fernandez and S. Sauter. Generalized convolution quadrature with variable time stepping. part II: Algorithm and numerical results. *Appl. Num. Math.*, 94:88–105, 2015.

[26] María López-Fernández and Stefan Sauter. Generalized convolution quadrature based on Runge-Kutta methods. *Numer. Math.*, 133(4):743–779, 2016. doi: 10.1007/s00211-015-0761-2.

[27] C. Lubich. Convolution quadrature and discretized operational calculus. I. *Numer. Math.*, 52(2):129–145, 1988.

[28] C. Lubich. Convolution quadrature and discretized operational calculus. II. *Numer. Math.*, 52(4):413–425, 1988.

[29] V. Mantič. A new formula for the C-matrix in the somigliana identity. *J. Elasticity*, 33: 191–201, 1993.

[30] M. Messner, M. Schanz, and J. Tausch. An efficient Galerkin boundary element method for the transient heat equation. *SIAM J. Sci. Comput.*, 37(3):A1554–A1576, 2015. doi: 10.1137/151004422. URL http://epubs.siam.org/toc/sjoce3/37/3.

[31] F. Neumann. *Vorlesung über die Theorie des Elasticität der festen Körper und des Lichtäthers*. Teubner, Leipzig, 1885.

[32] W. Nowacki. *Dynamic Problems of Thermoelasticity*. Nordhoff, Leyden, 1975.

[33] K.-H. Park and P. K. Banerjee. Two- and three-dimensional transient thermoelastic analysis by BEM via particular integrals. *Internat. J. Solids Structures*, 39(10): 2871–2892, 2002. ISSN 0020-7683. doi: 10.1016/S0020-7683(02)00125-7. URL http://www.sciencedirect.com/science/article/pii/S0020768302001257.

[34] H. Parkus. *Thermoelasticity*. Springer-Verlag, Wien, 2 edition, 1976.

[35] F. J. Rizzo and D. J. Shippy. An accurate boundary element method for the exterior elastic scattering problem in two dimensionsdvanced boundary integral equation method for three-dimensional thermoelasticity. *Int. J. Numer. Methods. Engrg.*, 11(11):1753–1768, 1977.

[36] S.A. Sauter and M. Schanz. Convolution quadrature for the wave equation with impedance boundary conditions. *J. Comput. Phys.*, 334:442–459, 2017. ISSN 0021-9991. doi: http://dx.doi.org/10.1016/j.jcp.2017.01.013. URL //www.sciencedirect.com/science/article/pii/S0021999117300232.

[37] Stefan Sauter and Christoph Schwab. *Boundary Element Methods*. Number 39 in Springer Series in Computational Mathematics. Springer Verlag, Heidelberg, 2011. doi: 10.1007/978-3-540-68093-2.

[38] M. Schanz. A boundary element formulation in time domain for viscoelastic solids. *Commun. Numer. Meth. Engng.*, 15:799–809, 1999.

[39] M. Schanz. Application of 3-d Boundary Element formulation to wave propagation in poroelastic solids. *Eng. Anal. Bound. Elem.*, 25(4-5):363–376, 2001.

[40] M. Schanz. *Wave Propagation in Viscoelastic and Poroelastic Continua: A Boundary Element Approach*, volume 2 of *Lecture Notes in Applied Mechanics*. Springer-Verlag, Berlin, Heidelberg, New York, 2001. doi: 10.1007/978-3-540-44575-3.

[41] S. Sharp and S. L. Crouch. Boundary integral methods for thermoelasticity problems. *J. of Appl. Mech.*, 53(2):298–302, 06 1986. ISSN 0021-8936. doi: 10.1115/1.3171755. URL https://doi.org/10.1115/1.3171755.

[42] V. Sládek and J. Sládek. Boundary integral equation method in thermoelasticity part I: General analysis. *Appl. Math. Modelling*, 7(4):241–253, 1983. ISSN 0307-904X. doi: 10.1016/0307-904X(83)90077-X. URL http://www.sciencedirect.com/science/article/pii/0307904X8390077X.

[43] V. Sládek and J. Sládek. Boundary integral equation method in thermoelasticity part III: Uncoupled thermoelasticity. *Appl. Math. Modelling*, 8(6):413–418, 1984. ISSN 0307-904X. doi: 10.1016/0307-904X(84)90047-7. URL http://www.sciencedirect.com/science/article/pii/0307904X84900477.

[44] Masa. Tanaka, T. Matsumoto, and M. Moradi. Application of boundary element method to 3-D problems of coupled thermoelasticity. *Eng. Anal. Bound. Elem.*, 16(4):297–303, 1995. ISSN 0955-7997. doi: https://doi.org/10.1016/0955-7997(95)00074-7. URL http://www.sciencedirect.com/science/article/pii/0955799795000747.

[45] Masataka Tanaka, Hidetoshi Togoh, and Masashi Kikuta. Boundary element method applied to 2-D thermoelastic problems in steady and non-steady states. *Eng. Anal. Bound. Elem.*, 1(1):13–19, 1984.

[46] N. Tosaka and I. G. Suh. Boundary element analysis of dynamic coupled thermoelasticity problems. *Comput. Mech.*, 8(5):331–342, Sep 1991. ISSN 1432-0924. doi: 10.1007/BF00369891. URL https://doi.org/10.1007/BF00369891.

[47] W. Weiß. *Thermische Auslegung von Werkzeugen für Presshärteprozesse*. PhD thesis, Graz University of Technology, 2013.